

www.acsami.org Research Article

Wafer-Scale Growth of 2D PtTe₂ with Layer Orientation Tunable High Electrical Conductivity and Superior Hydrophobicity

Mengjing Wang, Tae-Jun Ko, Mashiyat Sumaiya Shawkat, Sang Sub Han, Emmanuel Okogbue, Hee-Suk Chung, Tae-Sung Bae, Shahid Sattar, Jaeyoung Gil, Chanwoo Noh, Kyu Hwan Oh, YounJoon Jung, J. Andreas Larsson, and Yeonwoong Jung*



Cite This: ACS Appl. Mater. Interfaces 2020, 12, 10839-10851



Read Online

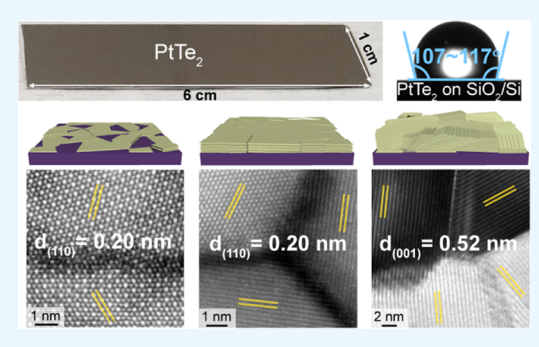
ACCESS

Metrics & More

Article Recommendations

Supporting Information

ABSTRACT: Platinum ditelluride (PtTe₂) is an emerging semimetallic two-dimensional (2D) transition-metal dichalcogenide (TMDC) crystal with intriguing band structures and unusual topological properties. Despite much devoted efforts, scalable and controllable synthesis of large-area 2D PtTe₂ with well-defined layer orientation has not been established, leaving its projected structure—property relationship largely unclarified. Herein, we report a scalable low-temperature growth of 2D PtTe₂ layers on an area greater than a few square centimeters by reacting Pt thin films of controlled thickness with vaporized tellurium at 400 °C. We systematically investigated their thickness-dependent 2D layer orientation as well as its correlated electrical conductivity and surface property. We unveil that 2D PtTe₂ layers undergo three distinct growth mode transitions, i.e., horizontally aligned holey layers, continuous layer-by-layer



lateral growth, and horizontal-to-vertical layer transition. This growth transition is a consequence of competing thermodynamic and kinetic factors dictated by accumulating internal strain, analogous to the transition of Frank—van der Merwe (FM) to Stranski—Krastanov (SK) growth in epitaxial thin-film models. The exclusive role of the strain on dictating 2D layer orientation has been quantitatively verified by the transmission electron microscopy (TEM) strain mapping analysis. These centimeter-scale 2D PtTe₂ layers exhibit layer orientation tunable metallic transports yielding the highest value of $\sim 1.7 \times 10^6$ S/m at a certain critical thickness, supported by a combined verification of density functional theory (DFT) and electrical measurements. Moreover, they show intrinsically high hydrophobicity manifested by the water contact angle (WCA) value up to $\sim 117^\circ$, which is the highest among all reported 2D TMDCs of comparable dimensions and geometries. Accordingly, this study confirms the high material quality of these emerging large-area 2D PtTe₂ layers, projecting vast opportunities employing their tunable layer morphology and semimetallic properties from investigations of novel quantum phenomena to applications in electrocatalysis.

KEYWORDS: 2D material, platinum ditelluride, PtTe₂, vertically aligned layers, hydrophobic, electrical conductivity

INTRODUCTION

Exploration of two-dimensional (2D) van der Waals (vdW) crystals based on transition-metal dichalcogenides (TMDCs) has inspired numerous innovations in a wide range of electronic applications. A primary emphasis has been driven to exploit their unprecedented electronic properties such as layer thickness-dependent opto-electrical tunablity^{1,2} and controlled manipulation of band structures for valleytronics.^{3,4} While semiconducting 2D TMDCs have been extensively studied as channels for digital electronics, their structural variations possessing metallic properties are gaining increasing interests. These materials are generally in the form of MX2 where M represents noble metals in place of refractory metals in 2D TMDCs and X represents chalcogen elements. Particularly, platinum (Pt)-based 2D chalcogenides present a variety of appealing aspects absent in conventional 2D TMDCs including thickness-dependent semiconducting-to-metallic transition, superior air stability, and low synthesis temperature. $^{5-10}$ For example, 2D Pt diselenide (PtSe $_2$) of mono-to-few layers presents high carrier mobility and small bandgap energies suitable for broadband optics while metallic properties achieved with its large layer number can realize metal—semiconductor seamless in-plane 2D junctions. Among Pt-based 2D chalcogenides, Pt ditelluride (PtTe $_2$) is an emerging material, which has been identified to possess unusual band structures and topological properties. Recent experiments report that 2D PtTe $_2$ is a type-II Dirac semimetal with a strongly tilted Dirac cone along Γ -A direction, projecting intriguing quantum phenomena such as anisotropic magnetism and topological transition. Moreover,

Received: December 2, 2019 Accepted: February 11, 2020 Published: February 11, 2020



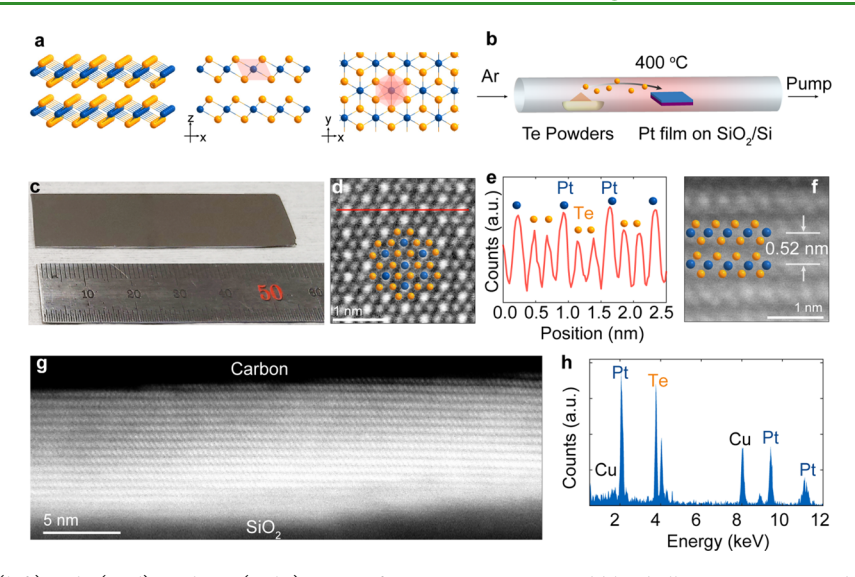


Figure 1. (a) Perspective (left), side (mid), and top (right) views of 1T-PtTe₂. Orange and blue balls represent Te and Pt atoms, respectively. The pink-shaded areas in the side and top views illustrate an octahedron atomic configuration. (b) Schematic illustration of the 2D PtTe₂ layer growth apparatus and procedure. (c) Camera image of a PtTe₂ sample on a SiO₂/Si wafer with a size of 1 cm × 6 cm. (d) Plane-view HAADF-STEM image of a 2D PtTe₂ basal plane. (e) Intensity profile corresponding to the red line in (d). (f) Cross-sectional HAADF-STEM image of 2D PtTe₂ layers with an interlayer spacing of 0.52 nm. (g) Representative cross-sectional STEM image of large-area, horizontally aligned 2D PtTe₂ multilayers. (h) EDS spectrum revealing a stoichiometry of Pt/Te = 1:2.

the theory predicts that it transits to a semiconductor with a small bandgap of $\sim\!\!0.4$ eV only when it is in a monolayer form. 20 Furthermore, an unusually high electrical conductivity of $\sim\!\!10^6\!-\!10^7$ S/m and large break-down current density have been observed in chemically synthesized PtTe₂ crystals. $^{21-23}$ In addition to this intrinsically semimetallic nature, 2D PtTe₂ is projected to exhibit high chemical reactivity suitable for hydrogen evolution reaction, 24,25 further justifying its rich novelty beyond conventional 2D TMDCs.

Despite such projected advantages, scalable and controllable chemical synthesis of 2D PtTe2 with well-defined layer orientation and material properties has not been established so far. Accordingly, a systematic understanding of its structure-property-process relationship has been lacking, impeding to unveil a full range of its intriguing attributes. Existing methods for fabricating 2D PtTe, layers include (1) chemical vapor transport growth of bulk PtTe2 crystals at 1000 °C through self-reflux and subsequent mechanical exfoliation, 25 (2) simultaneous evaporation of platinum tetrachloride (PtCl₄) or Pt and tellurium (Te) powders at a temperature range of ~800-1100 °C, ^{21,22} and (3) eutectic liquid synthesis of Pt-Te solid solutions at 700 °C.²³ A major drawback common in these approaches is that they yield 2D PtTe₂ layers of limited size (i.e., typically $\sim 5-20 \mu m$) as well as uneven spatial distribution and surface coverage. Moreover, the adopted synthesis temperature is high and even comparable to those for conventional 2D TMDCs (e.g., 2D molybdenum disulfide) despite the much lower melting temperature of Pt over refractory metals (e.g., Mo).²⁶

In this study, we report a low-temperature growth of 2D PtTe₂ layers on a large area greater than a few square centimeters by reacting Pt thin films of controlled thickness with vaporized Te at 400 °C. We systematically studied the thickness dependency of their growth orientation on resulting structural and electrical properties via comprehensive scanning transmission electron microscopy (STEM), X-ray diffraction (XRD), and electrical characterization. We unveil that 2D PtTe₂ layers accompany thickness-dependent distinct growth

modes: (1) layer-by-layer horizontal growth, (2) transition of horizontal-to-vertical layer orientation, and (3) mixture of horizontal and vertical growth. The underlying growth mechanism is discussed in the context of competition between growth kinetics and strain energy release, analogous to the transition of Frank-van der Merwe (FM) to Stranski-Krastanov (SK) growths established in three-dimensional (3D) epitaxial thin-film models. We also characterized the electrical conductivity of these orientation-controlled 2D PtTe₂ layers and identified its thickness dependency. 2D PtTe₂ multilayers of an optimum thickness exhibit the highest conductivity of $\sim 1.7 \times 10^6$ S/m, which is attributed to the excellent structural homogeneity of all horizontally aligned 2D layers as evidenced by cross-sectional STEM and XRD. The conductivity gradually decreases with increasing thickness while it still remains to be superior to those of any previously developed 2D TMDCs. 27-29 This thickness-dependent electrical property in conjunction with the variation of 2D layer orientation indicates a pronounced contribution of out-ofplane electron transports with increasing 2D vertical alignment. Finally, we performed water contact angle (WCA) measurements with 2D PtTe2 layers of varying thickness and identified their surface wettability. An intrinsically high hydrophobicity was identified by a large WCA value up to ~117°, significantly higher than the values observed with other 2D TMDCs of comparable lateral dimensions. 30-32 These comprehensive studies suggest the high structural and electrical quality of centimeter-scale 2D PtTe2 layers and unveil an exclusive role of their layer orientation on governing such attributes.

■ RESULTS AND DISCUSSIONS

2D dichalcogenides employing group X noble metals such as PtSe₂ and PtTe₂ preferably adopt the 1T configuration rather than the 2H. Figure 1a illustrates that 1T-PtTe₂ possesses a space group of *P3m1* as presented in its perspective (left), side (mid), and top (right) views. Each Te-Pt-Te layer constitutes edges-connected octahedra, with one representative octahedron as outlined in the pink regions of the side and top

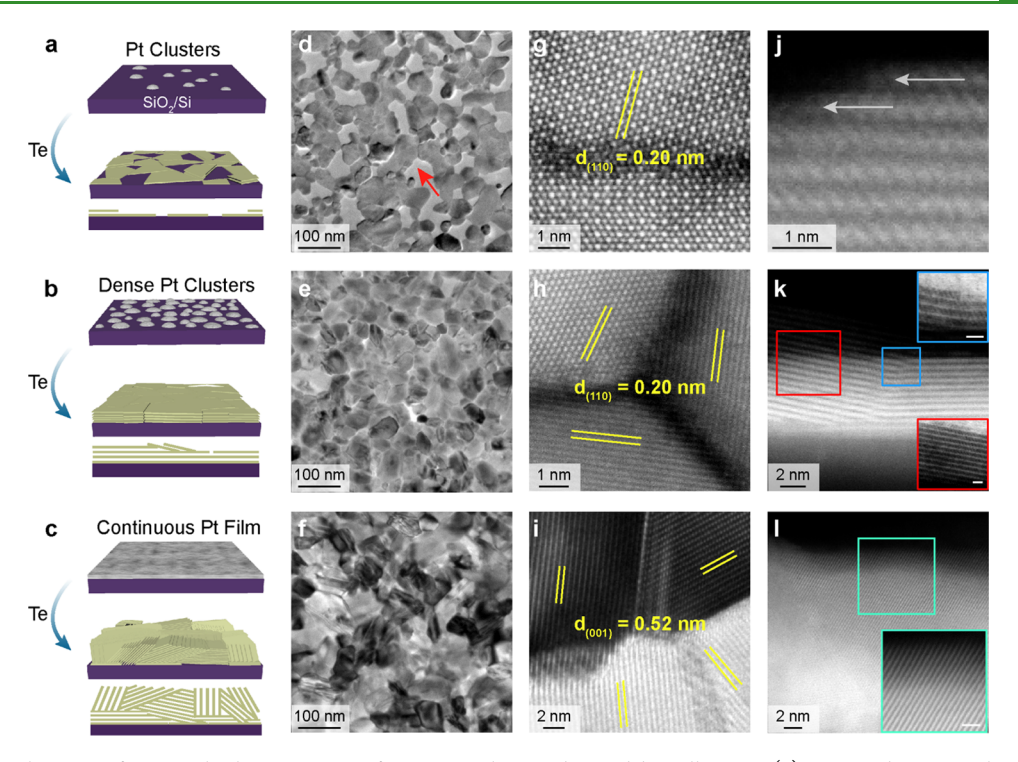


Figure 2. (a–c): Schematics for growth characteristics of 2D PtTe₂ layers obtained by tellurizing (a) scattered Pt nanoclusters, (b) dense Pt nanoclusters, and (c) continuous Pt films. The mid and bottom rows of (a, b, and c) represent projected and side-views of resulting 2D PtTe₂ layers, respectively. (d–f): HAADF-STEM images of (d) holey layers with the pores indicated by the red arrow, (e) continuous layers, and (f) continuous layers with pronounced imaging contrast. (g–i): High-resolution HAADF-STEM images of (g) (110) lattice fringes in crystalline grains with a grain boundary, (h) (110) lattice fringes from crystalline 2D basal planes of three distinct orientations, and (i) (001) lattice fringes denoting 2D layer vertical orientation. (j–l): Cross-sectional STEM images of (j) edge-terminated horizontally aligned 2D layers, (k) reorientation of 2D layers along with the top and bottom insets corresponding to the blue and red boxed regions, and (l) vertically aligned 2D layers along with the inset corresponding to the green boxed region. The scale bars of the insets are 1 nm.

views. Figure 1b illustrates the schematic setup and the procedure for 2D PtTe₂ layer growth. SiO₂/Si wafers covered with Pt films of a controlled thickness (i.e., $\sim 0.5-15$ nm) are reacted at 400 °C with vaporized Te under a continued supply of Argon (Ar) flow gas. Details for growth conditions are presented in the Methods Section. Figure 1c shows an image of a SiO₂/Si substrate with as-grown 2D PtTe₂ layers (1 cm \times 6 cm). Figure 1d shows a representative high angle annular darkfield (HAADF) STEM image of a 2D PtTe₂ basal plane revealing its 1T configuration. Figure 1e shows the intensity profile along the red line in Figure 1d, indicating the periodic spatial distribution of Pt and Te atoms. The superimposed atomic configuration in Figure 1d and the intensity fluctuation in Figure 1e are fully consistent with the atomic model presented in Figure 1a. Figure 1f shows a representative crosssection STEM image of 2D PtTe, layers revealing a stacking sequence of 1T Te-Pt-Te atomic chains with an interlayer spacing of 0.52 nm corresponding to the lattice constant c. Figure 1g shows a large-area STEM image of 2D PtTe₂ multilayers with horizontally aligned layers of high homogeneity, highlighting their excellent crystallinity and layer orientation control. The corresponding low-magnification cross-sectional TEM image is presented in Supporting Information, Figure S1, which confirms their large-area homogenous morphology without any discontinuity. Energydispersive X-ray spectroscopy (EDS) in Figure 1h further validates that the synthesized 2D PtTe2 layers possess a stoichiometry of Pt/Te = 1:2. Additional EDS spectra (Supporting Information, Figure S2), elemental mapping images (Supporting Information, Figure S3), and EDS line

scan profiles (Supporting Information, Figure S4) were obtained from 2D PtTe $_2$ layers prepared with various Pt film thicknesses, i.e., from 0.5 to 15 nm. The data confirm that the Pt/Te = 1:2 stoichiometry is well retained irrespective of the variation in initial Pt thickness, indicating the complete conversion of Pt to 2D PtTe $_2$.

We systematically grew 2D PtTe₂ layers by tellurizing Pt films of varying thickness and characterized their morphological transition. Figure 2a—c illustrates the morphology of 2D PtTe2 layers obtained with Pt thin films in three different thickness regimes, i.e., small (e.g., ~0.5 nm) for Figure 2a, intermediate (e.g., $\sim 1-3$ nm) for Figure 2b, and large (e.g., >6nm) for Figure 2c. These values denote the "nominal" thickness of deposited Pt films set by their e-beam evaporation conditions, and its correlation with the experimentally verified actual thickness of 2D PtTe2 layers is to be presented in the following section. In conjunction with the thickness variation of Pt films, three different growth modes have been observed. Growth mode (i) in Figure 2a: Holey PtTe2 films composed of horizontally aligned 2D layers are obtained by tellurizing Pt films of ~0.5 nm thickness. This is a consequence that depositing Pt films of such a small thickness form scattered Pt nanoclusters of low areal density (top). As a result, 2D PtTe2 layers grow without entirely covering the substrate surface (mid and bottom). Growth mode (ii) in Figure 2b: Continuous PtTe2 films composed of all horizontally aligned 2D layers are obtained by tellurizing Pt films of $\sim 1-3$ nm thickness. Tellurizing Pt nanoclusters of a much higher area density (top) convert them to continuous 2D PtTe2 layers, which laterally expand covering the free spaces on the substrate

(mid and bottom). Growth mode (iii) in Figure 2c: Continuous PtTe₂ films constituting a mixture of horizontally and vertically aligned 2D layers are obtained by tellurizing continuous Pt films of >6 nm thickness (top). Conversion of the continuous Pt films to 2D PtTe2 layers involves a significant volume expansion since Pt atoms take in additional Te atoms as well as forming vdW physical gaps. Accordingly, growing 2D PtTe2 layers will experience a substantial amount of accumulating strain, and some of their crystalline domains will prefer to reorient 2D layers in a vertical manner to release the strain (mid and bottom). This growth event is similar to the recently observed and verified strain-driven vertical growth of 2D MoS₂ layers.³³ Figure 2d-l presents STEM characterization to verify the thickness-dependent 2D PtTe2 layer morphological transition. Figure 2d-f shows low-magnification STEM images of 2D PtTe2 layers obtained from various Pt thicknesses of ~0.5, ~3, and ~15 nm. Figure 2d reveals that 2D PtTe₂ layers indeed exhibit rich porosity (red arrow), while the others show their continuous film morphology. 2D PtTe₂ layers in Figure 2d present an average domain size of ~50 nm with a spatial coverage ratio of ~74%, supporting their conversion from scattered Pt nanoclusters of low density illustrated in Figure 2a. It is also noted that 2D PtTe2 layers grown from the larger Pt thickness (Figure 2e) exhibit higher STEM imaging contrast over the other (Figure 2f), indicating significant inhomogeneity of 2D layer orientation. Figure 2g-i presents HAADF-STEM characterization of 2D PtTe2 layers obtained with various Pt thickness. Figure 2g shows a highresolution HAADF-STEM image obtained from holey 2D PtTe2 layers, revealing highly crystalline domains along with a grain boundary. The measured lattice spacing of 0.20 nm corresponds to (110) lattice fringes exposed on PtTe2 basal planes, indicative of horizontally aligned 2D layers. Figure 2h shows a representative high-resolution HAADF-STEM image of continuous 2D PtTe2 layers obtained from Pt thin films of intermediate thickness. The image reveals three crystalline domains of distinct crystallographic orientation, while (110) lattice fringes are uniformly observed in each grain. This observation indicates that horizontally aligned individual 2D layers of distinct orientation laterally "stitch" in an in-plane manner, evidencing their layer-by-layer growth nature. Figure 2i shows a representative high-resolution HAADF-STEM image of 2D PtTe2 layers obtained from Pt thin films of a much larger thickness (15 nm, in this case). Unlike the other cases, which confirm the layer-by-layer stitching of horizontally aligned 2D layers, we note distinct lattice fringes corresponding to (001) planes confirmed by the measured spacing of 0.52 nm. This observation indicates that crystalline domains are formed in the way that 2D PtTe2 layers grow upright in a vertical orientation, as illustrated in Figure 2c. In Figure 2i, the crystalline domain on the upper right corner is on-axis with respect to 2D layer orientation, while the others are slightly offaxis, which results in location-dependent imaging contrast difference. Figure 2j-l presents representative cross-sectional STEM images highlighting the distinct growth mode and orientation transition in 2D PtTe2 layers. Figure 2j reveals a high-resolution STEM image of horizontally aligned 2D layers where the arrows denote laterally terminated 2D layers on their top surface, directly evidencing the layer-by-layer stitching growth mode. Figure 2k displays a local area on 2D PtTe2 multilayers of ~10 nm thickness, evidencing the transition of horizontal-to-vertical layer orientation (blue and red insets). Figure 2l shows a representative cross-sectional STEM image

of 2D PtTe₂ multilayers of larger thickness. The inset reveals crystalline domains composed of vertically slanted 2D layers that expose their edge sites on the surface, corresponding to the in-plane STEM image in Figure 2i. The additional cross-sectional TEM image of 2D PtTe₂ layers obtained from the tellurization of a thick Pt film (\sim 15 nm) can be found in Supporting Information, Figure S5. Despite the growth mode variation, the average size of individual 2D PtTe₂ layer particles is nearly similar, i.e., \sim 40–60 nm, irrespective of the variation in initial Pt thickness (Supporting Information, Figure S6), which is attributed to the similar size distribution of individual Pt nanoparticle obtained with identical e-beam deposition conditions.

As above mentioned, 2D PtTe₂ layers below a certain critical transition point predominantly possess horizontally aligned layers. Accordingly, they are anticipated to exhibit Moiré patterns within crystalline domains of distinct crystallographic orientation, a decisive signature of layer-by-layer stacking of multiple 2D basal planes.³⁴ Figure 3a illustrates the generation

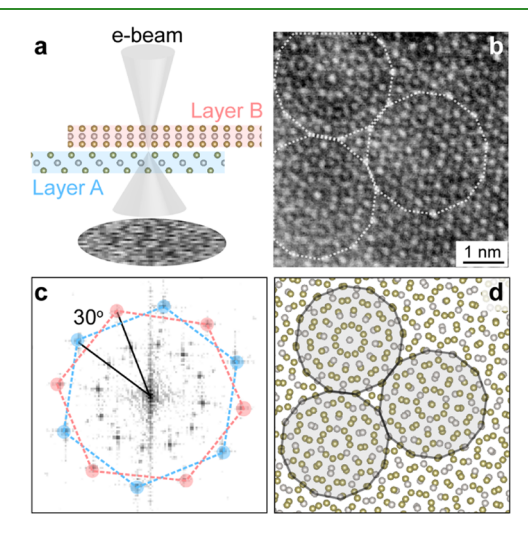


Figure 3. (a) Schematic illustration for the observation of Moiré patterns from an overlapping region of two horizontally aligned 2D PtTe2 layers with a misorientation angle of 30° under STEM mode. (b) HAADF-STEM images of a region exhibiting Moiré patterns obtained from horizontally aligned 2D PtTe2 layers prepared with Pt of $\sim\!0.5$ nm. (c) Corresponding FFT of (b) revealing two different sets of diffraction spots with a misorientation angle of 30°, matching with the layer configuration illustrated in (a). (d) Atomic simulation of Moiré patterns corresponding to the layer configuration described in (a). The black-outlined regions in (d) are entirely consistent with the white outlined regions in (b).

of Moiré patterns at STEM mode from horizontally aligned 2D PtTe $_2$ layers obtained from Pt thickness of \sim 0.5 nm with a misorientation angle between bottom layer A and top layer B. Figure 3b is a representative DF-STEM image of horizontally aligned 2D PtTe $_2$ layers exhibiting a Moiré pattern, as evidenced by the white dashed dodecagon circling out three subgroups of atoms with similar periodic arrangements. The corresponding fast Fourier transform (FFT) pattern in Figure 3c reveals two sets of hexagonally packed diffraction spots with a separation of 30° as differentiated by the blue and red shading, indicating two overlapping 2D horizontal basal planes with a misorientation angle of 30°. To substantiate the origin of Moiré pattern in Figure 3b, an atomic simulation of two horizontally stacked monolayers with a misorientation angle of

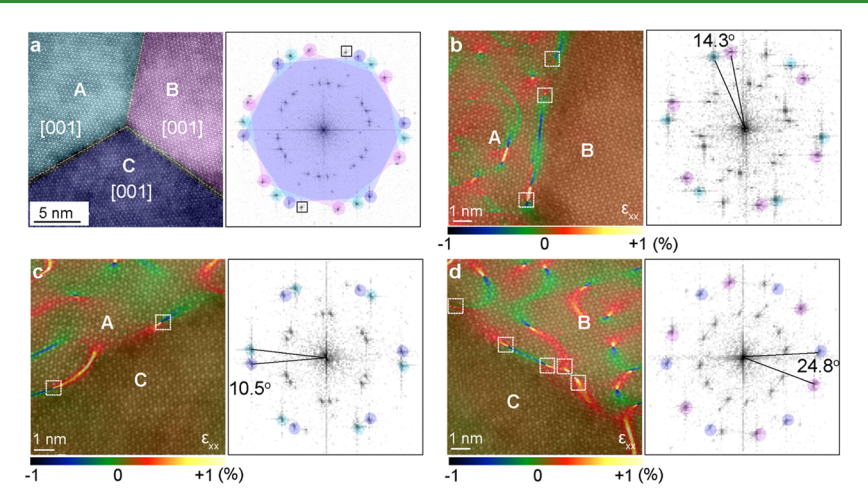


Figure 4. (a) DF-STEM image (left) and corresponding FFT pattern (right) of horizontally aligned 2D PtTe₂ multilayers constituting three crystalline grains composed of basal planes with distinct orientations. The blue, cyan, and pink-shaded spots in the FFT correspond to the grains denoted by the identical color in the DF-STEM image. The black squared diffraction spots in the FFT originate from the layer underneath the grains of A, B, and C. (b-d) GPA mapping and corresponding FFTs of grain boundaries formed by grains of (b) A + B, (c) C + A, and (d) B + C. The white dashed squares in (b-d) denote the dislocation cores exhibiting high strain.

30° is generated in Figure 3d. Three dodecagons blackoutlined in Figure 3d are the representative periodic patterns found in the Moiré pattern, corresponding to the white dodecagons highlighted in the STEM image of Figure 3b. Excellent agreement is observed between the experimental observation and the atomic simulation, which further verifies the layer-by-layer stitching growth dominantly observed in horizontally aligned 2D PtTe₂ layers.

The underlying mechanism, which dictates the thicknessdependent orientation transition of 2D PtTe2 layers, is discussed in the context of competition between thermodynamic and kinetic driving forces. In general, the growth of 2D PtTe2 layers should be driven to lower its associated thermodynamic energy, while it is simultaneously limited by the diffusion kinetics of Te atoms and the tellurization reaction rate. The growth mode (i) employs the tellurization of scattered and well-exposed Pt nanoclusters, which must be highly reactive, imposing low diffusion barriers for Te atoms. Thus, the kinetic effect should be insignificant, and the thermodynamic driving force favors to expose 2D basal planes of low surface energy, resulting in horizontally aligned 2D PtTe2 layers. While the surface coverage and dimension of Pt clusters are further increased (growth mode (ii)), the horizontal growth mode is still retained owing to a sufficient amount of free volumes in between them. Accordingly, 2D PtTe₂ multilayers of high structural homogeneity and full coverage are generated upon tellurizing Pt films of a certain critical thickness, as demonstrated in Figure 1g. Beyond this critical point where thicker Pt films become tellurized, a substantial amount of internal strain will start to accumulate particularly along the grain boundaries of 2D PtTe2 layers where 2D layers of distinct orientation converge. To release this additional strain energy during the course of continued growth, 2D PtTe2 layers start to adjust their layer orientation off the horizontal direction by entering the growth mode (iii). Given the high density and volume of Pt films in this case, diffusion of Te atoms into them becomes challenging and rate limiting compared to growth mode (ii) at such a low growth temperature of 400 °C. Accordingly, the growth mode (iii) is believed to be driven by kinetic factors, as verified by the significantly faster diffusion of chalcogen atoms along the

surface-exposed vdW gaps of vertically aligned 2D layers over 2D basal planes. 30,35,36

We note that this thickness-dependent transition of PtTe₂ layer orientation from "2D-like horizontal" to "3D-like vertical" is analogous to the growth characteristics established in 3D epitaxial thin films, i.e., the transition from Frank-van der Merwe (FM) growth to Stranski-Krastanov (SK) growth. 37,38 Despite the seemingly similar characteristics, it is necessary to point out that the growth principles for the conventional thinfilm epitaxy vs. 2D PtTe2 layer growth are fundamentally different at molecular levels. The epitaxial growth adopted in conventional thin-film technologies such as molecular beam epitaxy generally relies on the deposition and crystallization of gaseous molecular precursors. Meanwhile, the growth of 2D PtTe2 layers proceeds through the transformation of solidphase Pt films through their reaction with gaseous tellurium. 2D PtTe2 layers grown from the tellurization of thin Pt films preferably expose 2D basal planes of high atomic packing density, lowering the total thermodynamic energy. This event is akin to the FM mode, which predicts 2D layer-by-layer growth accompanying the exposure of atomically smooth and fully covered surfaces, as previously verified in thin-film epitaxial growth studies.³⁹ Following the initial growth of 2D multilayers driven by the FM mode, a nontrivial amount of strain energy subsequently accumulates particularly across sites of high structural inhomogeneity. 37,38,40 Above a certain layer thickness, this strain leads to a transition of FM-to-SK growth mode forming Volmer-Weber islands (vertically aligned 2D layers, in this case), which are energetically more favorable.⁴¹ This 3D thin-film epitaxy model well matches the growth characteristics observed with our 2D PtTe, layers of varying thickness, explaining the existence of a certain critical Pt thickness regime (~1-3 nm) above which vertically aligned 2D layers start to emerge.

The above growth mechanism analysis indicates the presence of a substantial amount of internal strain exerted by 2D layers of distinct crystallographic orientation. We hypothesize that such strain should significantly accumulate along the grain boundaries where 2D PtTe₂ layers with distinct orientations impeach each other during lateral volume expansion. To experimentally verify this prediction, we

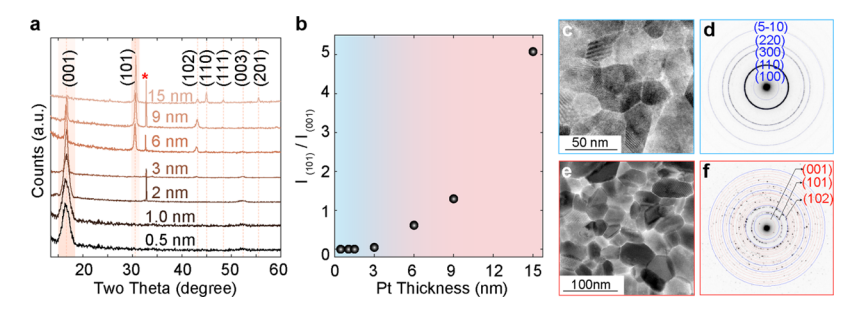


Figure 5. (a) XRD characterization of 2D PtTe₂ layers grown from Pt films of varying thickness. The red star mark denotes peaks from the growth substrate. (b) XRD peak intensity ratio of $I_{(101)}/I_{(001)}$ as a function of Pt film thickness. (c) Representative STEM image of crystalline grains constituting horizontally aligned 2D PtTe₂ layers. (d) Corresponding SAED pattern indicating that the indexed diffraction rings are normal to the [001] zone axis. (e) Representative STEM image of crystalline grains constituting a mixture of horizontally and vertically aligned 2D PtTe₂ layers. (f) Corresponding SAED pattern indicating a presence of both [001] and [101] zone axes. The blue highlighted diffraction rings correspond to those presented in (d), highlighting the crystallographic distinction of horizontally vs. vertically aligned 2D PtTe₂ layers.

employed a strain mapping analysis through geometric phase analysis (GPA)^{42,43} to the STEM images of horizontally aligned PtTe2 layers obtained with Pt of 1 nm thickness, right below the regime where vertically aligned 2D layers dominantly emerge. Figure 4a shows a representative DF-STEM image (left) from a location rich with grain boundaries formed by three distinct grains (denoted A, B, and C) as well as its corresponding FFT image (right). Three sets of hexagonally packed diffraction spots distinguished by the color shading in the FFT correspond to each individual grain in the STEM image. Figure 4b-d demonstrates the spatial strain distribution along the three sets of grain boundaries formed by grains of A-B (Figure 4b), C-A (Figure 4c), and B,C (Figure 4d) as well as their corresponding FFTs. We identify that dislocations with displacements of atoms are localized along the grain boundaries of high strain concentration, consistent with other GPA studies of dislocations. 44,45 In the strain mapping images of Figure 4b-d, the white squares denote the areas where dislocations under high strains are localized, manifested by the dark blue and bright yellow color. It is noteworthy that a larger misorientation angle between grains yields a higher linear density of dislocation cores at the grain boundaries. For instance, the areal density of dislocation cores associated with the misorientation angle of 24.8° (Figure 4d) is noticeably higher than that with 10.5° (Figure 4c). The observation is consistent with recent studies on the strain distribution along the grain boundaries within horizontally stacked 2D MoS2 layers, evidenced by the identical GPA method.44 This analysis directly evidences a significant amount of strain accumulation globally occurring within these intrinsically polycrystalline 2D PtTe₂ layers. A histogram of misorientation angles between individual grains was obtained from the sample prepared with the Pt film of 0.5 nm (Supporting Information, Figure S7), which indicates an absence of specifically preferred angle values. Furthermore, it is worth pointing out that the strain effect should become more pronounced with growths from Pt films of larger thickness accompanying larger grain sizes (XRD grain size analysis in Supporting Information, Figure S8).

To further elucidate the thickness-dependent crystallographic transition of 2D PtTe₂ layers, we employed diffraction characterization techniques, including X-ray diffraction (XRD) and TEM electron diffraction. Figure 5a,b shows XRD characterization of 2D PtTe₂ layers obtained from Pt films of varying thickness. With small enough thickness (<6 nm), 2D PtTe₂ layers preferably adopt horizontally aligned layers. This

is evidenced by the strong (001) crystalline peaks in Figure 5a, indicating the dominant coverage of 2D basal planes on the growth substrate while weak (003) peaks also appear. With Pt films of larger thickness, 2D PtTe2 layers gradually start to adopt vertically aligned and slanted layers. Crystalline planes other than (001) and (003), such as (101), (102), (110), and (111), start to emerge, which becomes more pronounced with larger thickness. Interestingly, the 2D PtTe2 layers obtained from 15 nm Pt exhibit a strong (101) peak intensity with a significantly suppressed (001) peak, a sharp contrast to the characteristics observed in those with Pt thickness <6 nm. This observation indicates that vertically aligned 2D layers significantly dominate over horizontal orientation, consistent with the TEM observations in Figure 2i-l. Further quantification was carried out by measuring the XRD intensity ratio of (101) over (001) peaks as a function of Pt film thickness, as presented in Figure 5b. It is evident that there is a sharp increase in the peak intensity ratio entering the 6 nm regime and beyond, indicating an onset of horizontal-tovertical transition in 2D layer orientation as denoted by the blue and red shading, respectively. In addition to observed peak intensity attenuation, the (001) peak becomes more sharpened with increasing initial Pt film thickness, which is majorly contributed to the increase of crystallite size along (001) direction (Supporting Information, Figure S8). Moreover, XRD characterization was performed to a thick Pt film of 15 nm before and after its tellurization (Supporting Information, Figure S9). In the XRD data, Pt crystal peaks completely vanish and only PtTe₂ peaks appear after the tellurization, which further validates the complete conversion of Pt to 2D PtTe₂ layers even with this large Pt thickness. TEM selected area electron diffraction (SAED) analysis was carried out to correlate the macroscopic observation by XRD with the microstructure of 2D PtTe₂ layers. Figure 5c shows a representative STEM image of 2D PtTe2 layers obtained from 1 nm Pt thickness, belonging to the horizontal orientation regime. Figure 5d presents its corresponding SAED characterization revealing a strong (110) ring pattern along the [001] zone axis, which indicates the dominant exposure of 2D basal planes on the surface consistent with Figure 2h. Figure 5e shows a representative STEM image of 2D PtTe2 layers obtained from 6 nm Pt thickness, belonging to the horizontalto-vertical transition regime. Figure 5f presents its corresponding SAED characterization where the indexed diffraction patterns indicate a presence of both [001] and [010] zone axes, corroborating with the XRD result in Figure 5a.

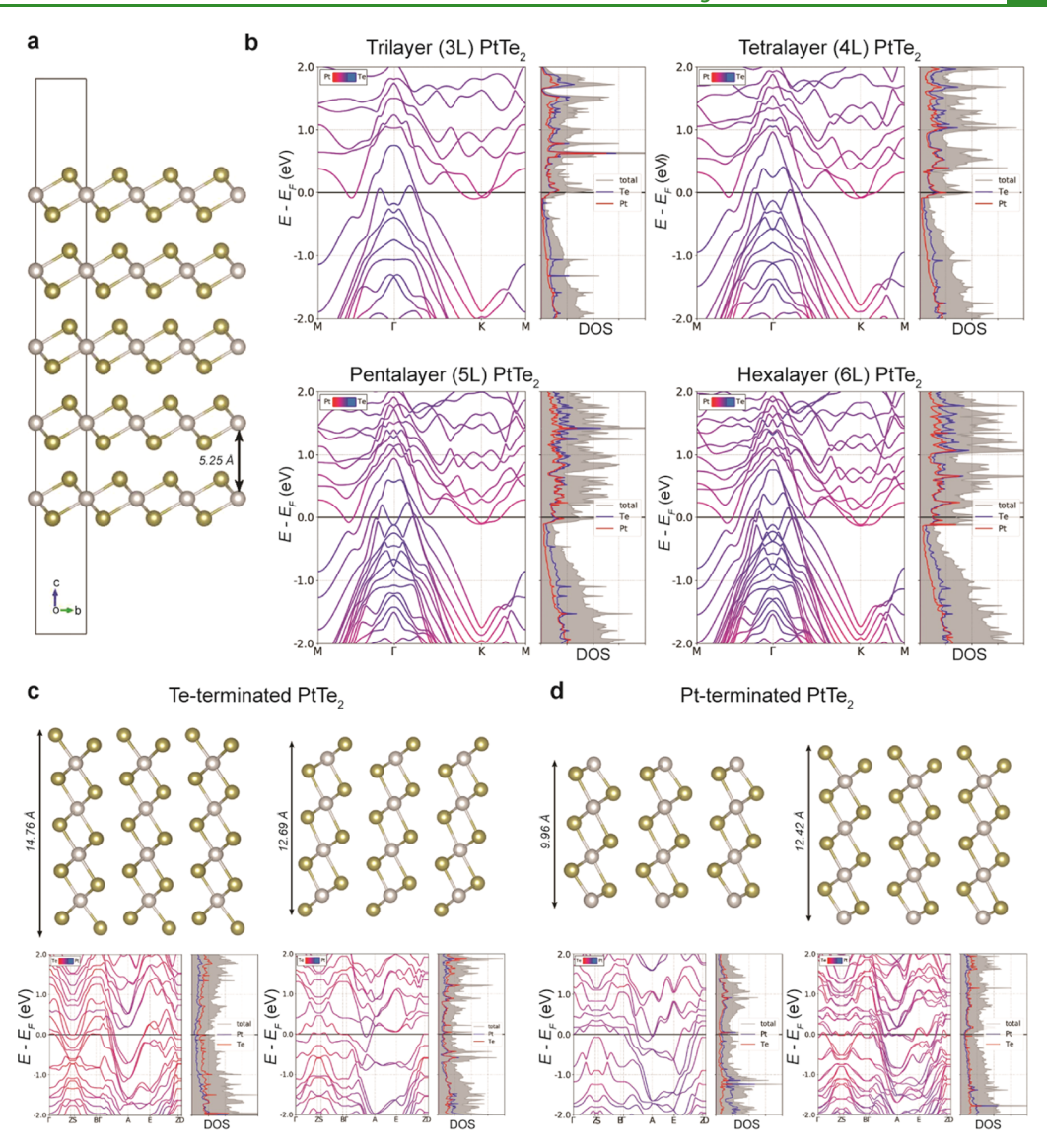


Figure 6. (a) Side view of pentalayer (5L) PtTe₂ as a representative system for horizontally aligned multilayers. (b) Electronic band structure and DOS plots for 3L-6L. (c) Side view (top) and electronic band structures (bottom) of vertically aligned 2D PtTe₂ with Te-terminated edge configurations. (d) Side view (top) and electronic band structures (bottom) of vertically aligned 2D PtTe₂ with Pt-terminated edge configurations.

From the above comprehensive structural characterization, we identified a thickness-dependent transition of 2D PtTe2 layer morphology and orientation, which indicates a possibility of thickness dependency in material properties such as electron transports. Herein, we systematically investigated electrical performances of 2D PtTe2 layers with varying thickness and identified a potential influence of 2D layer orientation on them, particularly of vertical orientation. We first identified their electronic band structures by performing first-principles calculations. To be consistent with the experimentally realized 2D PtTe₂ layer structures, we focused our calculations on horizontally aligned 2D PtTe2 multiple layers and vertically aligned 2D PtTe2 layers of varying lengths using the Vienna Ab-initio Simulation Package⁴⁶ (see Computational Details in the Methods Section). Horizontally aligned 2D PtTe₂ layers of varying layer numbers from trilayer (3L) to hexalayer (6L) are modeled, and Figure 6a shows a schematic view of representative pentalayer (5L) PtTe2. The optimized lattice constant a for 3L-6L PtTe2 turns out to be in the range of 4.045–4.051 Å with a Pt–Pt interlayer distance (d_{Pt-Pt}) of 5.25

Å, which is in close agreement to the experimentally observed value of 0.52 nm. Corresponding electronic band structures plotted along the high-symmetry line $(M - \Gamma - K - M)$ are given in Figure 6b, which clearly depicts the metallic nature of horizontally aligned 2D PtTe2 multilayers irrespective of their layer number. Furthermore, we show the atomic projected density of state (PDOS) plots and found mixed contributions from both Pt and Te atomic states around the Fermi level. We next address the case of vertically aligned 2D PtTe, layers, as shown in Figure 6c,d. Fixing the Pt-Pt interlayer distance to 5.25 Å identical to the case of horizontally aligned layers, we consider an orthorhombic unit cell of various edge configurations, i.e., Te-terminated edges in Figure 6c and Ptterminated edges in Figure 6d. The electronic band structures plotted along the high-symmetry line (Γ -Z-S-B- Γ -A-E-Z-D) in Figure 6c,d demonstrate the metallic behavior of vertically aligned 2D PtTe₂ layers regardless of edge configurations. This finding of the metallic nature of vertically aligned 2D PtTe2 layers remains unchanged even with further increasing their vertical layer length (Supporting Information, Figure S10).

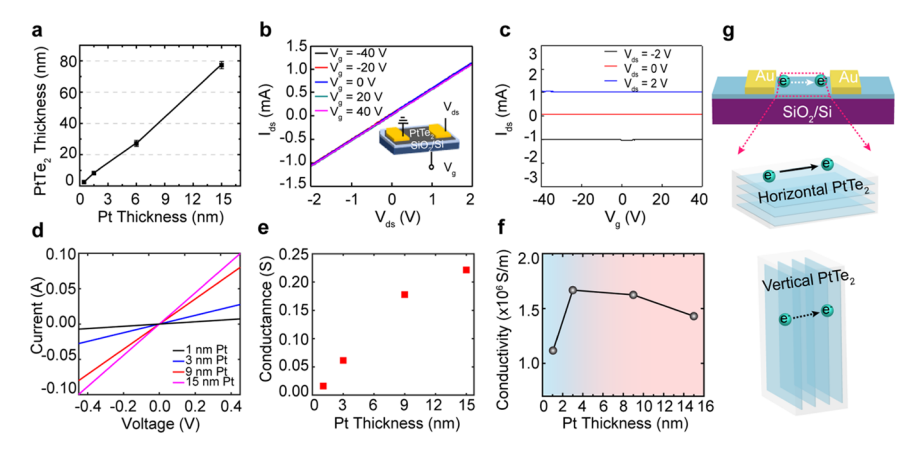


Figure 7. (a) Thickness of 2D PtTe₂ layers as a function of Pt thickness. (b, c) Back-gate FET measurements of 2D PtTe₂ layers obtained from ~0.5 nm Pt thickness, showing (b) I_{ds} – V_{ds} and (c) I_{ds} – V_{g} transfer characteristics. (d) I–V curves of 2D PtTe₂ prepared from various Pt thicknesses. (e) Conductance as a function of Pt thickness. (f) Conductivity as a function of Pt thickness showing a presence of its thickness-dependent maximum point. The junction of the blue and red shading represents a transition of horizontal-to-vertical layer orientation. (g) Schematics of electron transports in horizontally vs. vertically aligned 2D PtTe₂ layers.

For the sake of completeness, we also calculated the band structures of $PtTe_2$ in monolayer and bulk forms (**Supporting Information**, Figure S11). Consistent with previous density functional theory (DFT) studies, ²⁰ 2D $PtTe_2$ layers exhibit a bandgap of ~0.8 eV when they are in a monolayer form (Figure S3a,b) while they are metallic in a bulk form (Figure S4c,d). Indeed, it is known that 2D $PtTe_2$ layers are semiconducting only when they possess monolayers unlike other Pt-based 2D chalcogenides such as 2D $PtSe_2$, which can be still semiconducting with few-to-several layers. ⁴⁷

We then experimentally studied the thickness-dependent electrical performances of 2D PtTe2 layers. We first identified the relationship of Pt film thickness and resulting 2D PtTe2 layer thickness by performing atomic force microscopy (AFM) height profile measurements, as presented in Figure 7a. We note that the actual thickness of 2D PtTe2 layers is ~5 times larger than the nominal thickness of Pt films, which is set by the deposition conditions inherent to our e-beam evaporator. We then investigated the carrier type of as-grown 2D PtTe₂ layers on SiO₂/Si wafers by characterizing their field-effect transistor (FET) gate responses. From various theory studies²⁰ and our DFT calculation results, it is well established that 2D PtTe2 layers do not possess bandgap energies even in a fewlayer form. We thus focused our measurements on 2D PtTe₂ layers obtained from Pt films of a very small thickness (e.g., ~ 0.5 nm corresponding to a 2D layer thickness of ~ 2.5 nm), as presented in Figure 7b,c. Figure 7b shows transfer characteristics of drain-source voltage (V_{ds}) vs. drain-source current (I_{ds}) with varying back-gate voltage (V_g) , and Figure 7c shows I_{ds} – V_g at varying V_{ds} . As anticipated, 2D PtTe₂ layers reveal strong metallic characteristics, as manifested by the complete overlap of $I_{\rm ds}$ – $V_{\rm ds}$ irrespective of $V_{\rm g}$ (Figure 7b) and the V_g -independent I_{ds} (Figure 7c). The inset in Figure 7b illustrates a schematic of 2D PtTe2 layer-based FET in a backgate configuration. Having confirmed the intrinsically metallic nature of 2D PtTe2 layers, we investigated their thicknessdependent electron transports. For rigorous quantification, we precisely defined the geometrical dimension of 2D PtTe2 layers by AFM characterization of their actual thickness (Figure 7a) and by patterning gold (Au) electrodes with an identical channel length (width: 200 μ m, spacing: 100 μ m). The additional temperature-dependent measurement data in

Supporting Information, Figure S12 also confirms that 2D PtTe₂ layers present intrinsically metallic transports with nearly constant or slightly decreased conductivity with increasing temperature. Figure 7d shows I-V characteristics obtained from 2D PtTe2 layers of varying Pt thickness, and Figure 7e presents the corresponding electrical conductance obtained from their tangential slopes. Electrical conductivity was determined by combining the geometrical dimension with the measured conductance, and its thickness-dependency is presented in Figure 7f. With increasing Pt thickness, the conductivity steadily increases yielding the highest value of $\sim 1.7 \times 10^6$ S/m at ~ 3 nm thickness. This thickness is the critical point where 2D PtTe2 multilayers exhibit horizontally aligned layer orientation with full surface coverage and high structural homogeneity. The lower conductivity value from a smaller Pt thickness is attributed to their intrinsically holey morphology (Figure 2a,d). Beyond this critical point, vertically aligned 2D layers start to emerge as confirmed by the XRD (Figure 5a) and STEM/SAED (Figure 5c,d) characterization. With further increasing thickness, the conductivity gradually decreases reaching $\sim 1.4 \times 10^6$ S/m at Pt thickness of 15 nm. This thickness-dependent conductivity decrease well agrees with the thickness-dependent transition of 2D layer orientation, i.e., emergence of vertically aligned 2D layers beyond a certain critical thickness continuously becomes more pronounced with further increasing thickness (Figure 7a,b). This suppressed conductivity from the vertically aligned 2D layers is attributed to the increasing contribution of "out-ofplane" transports of electrons across vdW physical gaps, as illustrated in Figure 7g. This observation is well supported by previous experimental and theoretical studies that report much higher energy barriers for the electrons undergoing out-ofplane transports across vdW gaps over those traveling in an "inplane" manner. 48,49 It is also worth mentioning that the overall conductivity values are on the order of 106 S/m, highly comparable to those of previously reported 2D PtTe2 layers of much smaller dimensions, which fall in the range of $3.3-6.4 \times 10^6$ S/m (Supporting Information, Table S1). 21-23 Moreover, these conductivity values are significantly higher than those of any other 2D TMDC layers, e.g., the highest reported being vanadium diselenide (VSe₂) with a conductivity of $\sim 1 \times 10^6$ S/m⁵⁰ (Supporting Information, Table S1). Such an unusual

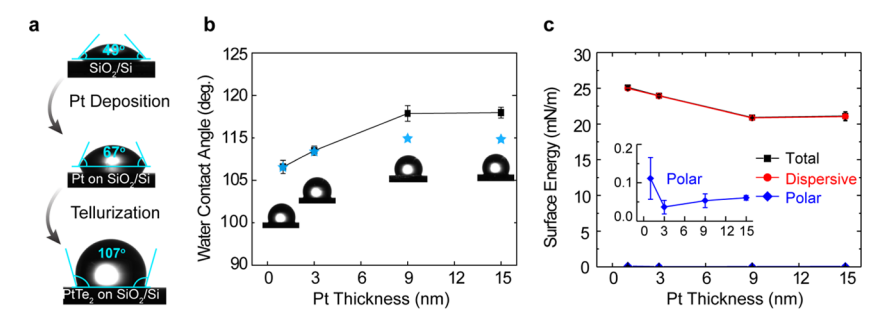


Figure 8. (a) Sequential water contact angle measurements of SiO₂/Si throughout Pt deposition and tellurization. (b) Thickness-dependent apparent WCA values of 2D PtTe₂ layers and their corresponding water droplet images. The blue stars mark the intrinsic water contact angles with consideration of surface roughness effects. (c) Thickness-dependent surface energy values incorporating polar and dispersive components.

Table 1. Water and DIM Contact Angle values for 2D PtTe₂ Layers with Different Thicknesses and Their Corresponding Surface Energy

		apparent CA $(heta_{ ext{a}})$		intrinsic CA (θ_i)		surface energy (mN/m)		
Pt thickness (nm)	roughness ratio (r)	water	DIM	water	DIM	$\gamma^{ m d}$	γ^{P}	γ
1	1.003	107.4 ± 1.2	66.6 ± 0.6	107.1	66.43	25.0	0.11	25.11
3	1.006	110.2 ± 0.8	69.1 ± 0.4	109.6	68.69	23.92	0.04	23.96
9	1.046	117.5 ± 1.5	77.5 ± 0.4	111.6	74.02	20.86	0.05	20.91
15	1.051	117.0 ± 0.9	77.4 ± 1.2	111.3	73.61	21.06	0.06	21.12

combination of extremely high electrical conductivity, waferscale dimension, and tunable geometry offers numerous opportunities beyond applications of electronics, e.g., electrochemical or catalytic applications requiring high electrical conductivity coupled with large structural porosity and surface area.

In addition to the electrical aspect, we also characterized surface properties of the large-area 2D PtTe2 layers to gain additional insights regarding their material quality. We identified the water wettability of as-grown 2D PtTe2 layers on SiO₂/Si substrates of varying thickness by measuring their water contact angle (WCA) values. Figure 8a shows representative images of water droplets on a bare SiO₂/Si wafer (top), after Pt deposition (mid), and after 2D PtTe2 layers growth (bottom). The bare SiO₂/Si growth substrate exhibits a WCA value of ~49° indicating its intrinsic hydrophilicity, which turns to strong hydrophobicity after 2D PtTe₂ layer growth, manifested by the large WCA values (typically > 100°). Figure 8b presents thickness-dependent WCA values of 2D PtTe₂ layers, which confirms their intrinsically strong hydrophobicity irrespective of thickness. Remarkably, these values are much higher than those observed with any other 2D materials, including 2D TMDCs and graphene. 31,51,52 Indeed, the WCA value of $\sim 110^{\circ}$ observed with 2D PtTe2 multilayers in a fully horizontal orientation (i.e., Pt thickness ~3 nm) is the largest among those previous reports on any horizontally stacked 2D materials (i.e., 98° of MoS₂³⁰ and 83° of WS₂³¹) without surface modifications (Supporting Information, Table S2), suggesting their superior hydrophobicity and crystal quality. The lower WCA value observed with 2D PtTe₂ layers prepared from Pt < 3 nm is attributed to their intrinsic holey morphology, contributed by the exposed SiO₂/Si surface, which is intrinsically hydrophilic (Figure 8a). The pronounced transition of horizontal-tovertical 2D layer orientation beyond 3 nm Pt (Figure 8a,b) steadily increases WCA values with increasing thickness, similar to the trends observed with 2D MoS₂ layers.^{53,54} The surface wettability of a thin film strongly depends on its surface

chemistry and topographical morphology, as expressed by the Wenzel equation. 55

$$\cos \theta_{\rm a} = r \cos \theta_{\rm i} \tag{1}$$

In the equation, r is its roughness ratio (i.e., the ratio of the actual area/projected area) and θ_a , θ_i are its apparent and intrinsic CA values, respectively, which greatly vary with the kind of integrated droplets. Using eq 1, we calculated the "intrinsic" CA values of 2D PtTe, layers and marked with blue stars in Figure 8b, which reflect their surface wettability under the condition that the surface is completely flat. The surface roughness ratio of 2D PtTe2 layers with varying Pt thickness was determined by AFM topography measurements (Supporting Information, Figure S13). Table 1 presents the intrinsic CA values of 2D PtTe2 layers determined by droplets of diiodomethane (DIM). It is noted that the intrinsic CA values do not exhibit much difference irrespective of thickness. indicating that the "intrinsically" high hydrophobicity of 2D PtTe₂ layers is not a result of their surface roughness. To better understand the origin of this unique high hydrophobicity unattainable in any other 2D TMDCs, we measured the surface energy of 2D PtTe2 layers using the Owens-Wendt method⁵⁶ and presented it in Figure 8c. The surface energy is a summation of two contributing components, one is a polar component, which depicts the interaction of a material with permanent or induced dipoles, and the other is a dispersive component, which reflects a nonpolar interaction such as London dispersive force. It is interesting to note that the surface tension of 2D PtTe2 layers is nearly composed of only nonpolar components ($\gamma^d \sim 20-25 \text{ mN/m}$) with a negligible contribution from the polar component (γ^p < 0.1 mN/m) irrespective of their thickness. This observation indicates that 2D PtTe₂ layers exhibit intrinsically low polarity, which is attributed to the similar electronegativity values of Pt (\sim 2.28) and Te (~2.10) in the Pauling scale. 57,58 Indeed, this low electronegativity difference of ~0.18 is the smallest for any Ptbased TMDCs, indicating the dominance of nonpolar covalent bonds between Pt and Te atoms. 57,58

CONCLUSIONS

To conclude, we report a scalable growth of 2D PtTe2 layers at a low temperature of 400 °C by tellurizing Pt films of controlled thickness. We observed their thickness-dependent transition of layer morphology and orientation, confirmed by extensive TEM, STEM, XRD, and electron diffraction characterization. The transition is identified to result from a competing interplay of thermodynamic and kinetic factors where an internal strain accumulating during the course of 2D layer growth plays a critical role. This thickness-dependent morphological transition in 2D PtTe2 layers is correlated with their electrical conductivity, which exhibits a maximum at a certain critical thickness regime after which it steadily decreases. The electrical conductivity values of 2D PtTe2 layers, as well as their WCA values, are much higher than those of any other previously explored 2D TMDCs, confirming high material quality. Accordingly, this study is believed to pave the way for investigations of novel quantum phenomena in this relatively less-explored Dirac semimetal of a large area.

METHODS

Synthesis of 2D PtTe₂ Layers. Pt seeds of controlled thickness were deposited on SiO_2/Si wafers (300 nm; SiO_2 thickness) by an electron beam evaporator (Thermionics VE-100) at a fixed evaporation rate of 0.15 Å/s. Pt-deposited SiO_2/Si substrates were placed in the center zone of a quartz tube inside a thermal furnace (Lindberg/Blue M Mini-Mite), and an alumina boat containing Te powder was placed at the furnace upstream side (temperature ~200 °C). Following Ar purging down to a base pressure of ~1 mTorr, the furnace subsequently ramped up to the growth temperature of 400 °C at a rate of 7.6 °C/min was maintained for 50 min. During the growth reaction, the flow rate of Ar gas was kept being ~100 standard cubic centimeters per minute (SCCM) at a pressure of ~80 mTorr.

TEM Characterization and Analysis. The structural and chemical integrity of as-grown 2D PtTe₂ layers was characterized using FEI F30 TEM (operation voltage: 300 kV) and JEOL ARM 200 F Cs-corrected TEM (operation voltage: 200 kV). For plane-view TEM sample preparation, the buffered oxide etchant was directly applied to as-prepared 2D PtTe₂-SiO₂/Si substrates and the separated 2D PtTe₂ layers were manually integrated onto copper TEM grids. Cross-sectional TEM samples were prepared using a focused ion beam (FIB: Quanta 2D FEG, FEI) employing Ga ion beam (30 keV)-based TEM lift-out techniques. The atomic simulation of the Moiré pattern was obtained by stacking two monolayers with a misorientation angle of 30° and was visualized in Vesta atomic visualization program. Geometrical phase analysis (GPA) of the HAADF-STEM image was performed using a built-in Digital Micrograph script.⁴²

XRĎ Characterization. X-ray diffraction of 2D PtTe₂ films on SiO_2/Si wafers was carried out by a PANalytical Empyrean diffractometer equipped with a copper X-ray source ($K\alpha 1 = 1.5406$ Å, $K\alpha 2 = 1.54439$ Å) and a Pixcel3D detector. Diffraction data were collected under an operation tension of 45 kV and a current of 40 mA using theta-two theta scan geometry.

Water Contact Angle and Surface Energy Measurement. The water contact angle of 2D PtTe₂ layers was measured with a goniometer (model 90, ramé-hart instrument co.) by sessile drop tests. Water droplets (2 μ L) were gently deposited on as-grown 2D PtTe₂ sample surfaces using a microsyringe, and the contact angle was extracted using the DROPimage Pro software (Ramé-Hart instrument co.). The average contact angle value was obtained from at least six different locations of each sample. Additionally, the contact angle of diiodomethane (DIM; CH₂I₂) was measured to determine the surface energy value using the following Owens—Wendt method. The surface energy (γ s) of a solid 2D layer is expressed to be the summation of two constituting components, i.e., dispersive (γ s) and

polar (γ_s^p) components $(\gamma_s = \gamma_s^d + \gamma_s^p)$. Also, the interfacial energy (γ_{sl}) between a 2D layer and a liquid is defined to be eq 2

$$\gamma_{sl} = (\sqrt{\gamma_s^d} - \sqrt{\gamma_l^d})^2 + (\sqrt{\gamma_s^p} - \sqrt{\gamma_l^p})^2$$
 (2)

where γ_i^d and γ_i^p are the dispersive and polar components of the liquid, respectively. Combining the above equation with Young's equation $\{\cos\theta=(\gamma_s-\gamma_l)/\gamma_s\}$, which is widely used to express the relation between the contact angle and interfacial energies in triple-phase systems, ⁵⁶ leads to eq 3

$$1 + \cos \theta = 2\sqrt{\gamma_s^d} \left(\frac{\sqrt{\gamma_l^d}}{\gamma_l} \right) + 2\sqrt{\gamma_s^p} \left(\frac{\sqrt{\gamma_l^p}}{\gamma_l} \right)$$
 (3)

By incorporating the measured contact angle values and known surface energy values 56 of water ($\gamma_1 = 72.8$, $\gamma_1^d = 21.8$, $\gamma_1^p = 51$ mN/m) and DIM ($\gamma_1 = 50.8$, $\gamma_1^d = 49.5$, $\gamma_1^p = 1.3$ mN/m) into the above equation, we can finally obtain the surface energy of the 2D layer in Figure 8c.

Electrical Characterization. All electrical measurements were performed with a home-built probe station using a HP 4156 A semiconductor parameter analyzer. Gold was evaporated on top of asgrown 2D PtTe₂ layers on SiO₂/Si substrates through a metal shadow mask for electrode patterning.

AFM Characterization. A tapping mode AFM (Anasys Instruments, NanoIR2) scanning was carried out to reveal the topography of 2D PtTe₂ layers at a scan rate of 0.3 Hz. The AFM probe (model: PR-EX-T125-10) has a resonant frequency of 200-400 kHz and a spring constant of 13-77 N/m.

Computational Details. We use density functional theory with the projector augmented wave method 59,60 as implemented in the Vienna Ab-initio Simulation Package. 46 The generalized gradient approximation in the Perdew-Burke-Ernzerhof parametrization is employed for the exchange-correlation potential, and the plane wave cutoff energy is set to a sufficiently large value of 420 eV. The vdW interaction is taken into account using the nonlocal optB86b-vdW density functional. A 7 -centered Monkhorst-Pack 12 \times 12 \times 1 (9 \times 9 \times 2) k-mesh is used for the structural relaxation, whereas for selfconsistent calculations, the Brillouin zone integration is performed using a dense $20 \times 20 \times 1$ (11 × 11 × 3) k-mesh for horizontally (vertically) aligned 2D PtTe2, respectively. We ensure an energy convergence of 10^{-6} eV and force convergence of 10^{-3} eV/Å for the iterative solution of the Kohn-Sham equations. Due to the constituent heavy elements involved in PtTe2, the effects of spinorbit coupling are always taken into account in our calculations. We also use a 15 Å thick layer of vacuum on top of both horizontally and vertically aligned 2D PtTe2 layers to exclude spurious interaction between periodic images in the out-of-plane direction as threedimensional periodic boundary conditions are applied. The results are plotted using the Matplotlib software package.

ASSOCIATED CONTENT

Supporting Information

The Supporting Information is available free of charge at https://pubs.acs.org/doi/10.1021/acsami.9b21838.

Characterization data including TEM, EDS, grain size analysis, XRD, DFT calculation, temperature-dependent conductivity measurement, AFM, and tables of water contact angles and electrical conductivities (PDF)

AUTHOR INFORMATION

Corresponding Author

Yeonwoong Jung — NanoScience Technology Center, Department of Electrical and Computer Engineering, and Department of Materials Science and Engineering, University of Central Florida, Orlando, Florida 32826, United States; orcid.org/0000-0001-6042-5551; Email: yeonwoong.jung@ucf.edu

Authors

Mengjing Wang — NanoScience Technology Center, University of Central Florida, Orlando, Florida 32826, United States; orcid.org/0000-0003-1195-4515

Tae-Jun Ko – NanoScience Technology Center, University of Central Florida, Orlando, Florida 32826, United States

Mashiyat Sumaiya Shawkat — NanoScience Technology Center and Department of Electrical and Computer Engineering, University of Central Florida, Orlando, Florida 32826, United States; ⊚ orcid.org/0000-0001-6594-190X

Sang Sub Han – NanoScience Technology Center, University of Central Florida, Orlando, Florida 32826, United States; Department of Materials Science and Engineering, Seoul National University, Seoul 08826, South Korea

Emmanuel Okogbue — NanoScience Technology Center and Department of Electrical and Computer Engineering, University of Central Florida, Orlando, Florida 32826, United States

Hee-Suk Chung — Analytical Research Division, Korea Basic Science Institute, Jeonju 54907, South Korea

Tae-Sung Bae – Analytical Research Division, Korea Basic Science Institute, Jeonju 54907, South Korea

Shahid Sattar — Applied Physics, Division of Materials Science, Department of Engineering Sciences and Mathematics, Luleå University of Technology, Luleå, SE 97187, Sweden;
ocid.org/0000-0003-4409-0100

Jaeyoung Gil – Department of Chemistry, Seoul National University, Seoul 08826, South Korea

Chanwoo Noh – Department of Chemistry, Seoul National University, Seoul 08826, South Korea

Kyu Hwan Oh – Department of Materials Science and Engineering, Seoul National University, Seoul 08826, South Korea

YounJoon Jung — Department of Chemistry, Seoul National University, Seoul 08826, South Korea; orcid.org/0000-0002-9464-9999

J. Andreas Larsson — Applied Physics, Division of Materials Science, Department of Engineering Sciences and Mathematics, Luleå University of Technology, Luleå, SE 97187, Sweden; orcid.org/0000-0003-3455-2877

Complete contact information is available at: https://pubs.acs.org/10.1021/acsami.9b21838

Author Contributions

M.W. and T.-J.K. contributed equally. Y.J. conceived the project and directed it. T.-J.K. synthesized 2D PtTe₂ films with the assistance of M.S.S., S.S.H., and E.O., M.W., S.S.H., T.-S.B., and H.-S.C. performed the TEM characterization under the guidance of Y.J., and K.H.O., M.W. performed the XRD characterization. T.-J.K., M.W., and M.S.S. performed the electrical characterization. M.W. performed the TEM strain mapping imaging and diffraction analysis. T.-J.K. performed the WCA measurement and its analysis. S.S.H., J.G., and C.N. performed the DFT calculation under the guidance of J.A.L, and Y.J.J., M.W., T.-J.K., and Y.w.J. wrote the manuscript with inputs from all authors.

Notes

The authors declare no competing financial interest.

ACKNOWLEDGMENTS

This work was supported by the National Science Foundation (CMMI-1728390) (M.S.S.), the Korea Institute of Energy Technology Evaluation and Planning (KETEP), and the Ministry of Trade, Industry & Energy (MOTIE) of the Republic of Korea (No. 20173010013340) (Y.J.). Y.J. also acknowledges the VPR Advancement of Early Career Researchers award from the University of Central Florida. S.S. and J.A.L. thank Knut och Alice Wallenberg foundation, Kempestiftelserna and Interreg Nord for financial support. S.S. and J.A.L. also thank High Performance Computing Center North (HPC2N), National Supercomputer Center in Linköping (NSC), and the PDC Center for High Performance Computing for allocation of time and resources, through the Swedish National Infrastructure for Computing (SNIC). This research was in part supported by the Creative Materials Discovery Program through the National Research Foundation of Korea (NRF) funded by the Ministry of Science, ICT and Future Planning (NRF-2017M3D1A1039553). S.S.H. and K.H.O. were supported by a grant [KCG-01-2017-02] through the Disaster and Safety Management Institute funded by the Korea Coast Guard of the Korean government. The work at Seoul National University was supported by the National Research Foundation of Korea (grant no. NRF-2018R1D1A1B07043973).

ABBREVIATIONS

PtTe₂, platinum ditelluride
2D, two-dimensional
TMDC, transition-metal dichalcogenide
FM, Frank—van der Merwe
SK, Stranski—Krastanov
TEM, transmission electron microscopy
STEM, scanning transmission electron microscopy
HAADF, high angle annular dark-field
DFT, density functional theory
WCA, water contact angle
XRD, X-ray diffraction
EDS, energy-dispersive X-ray spectroscopy
GPA, geometric phase analysis
AFM, atomic force microscopy

REFERENCES

- (1) Kwon, J.; Lee, J. Y.; Yu, Y. J.; Lee, C. H.; Cui, X.; Hone, J.; Lee, G. H. Thickness-Dependent Schottky Barrier Height of MoS₂ Field-Effect Transistors. *Nanoscale* **2017**, *9*, 6151–6157.
- (2) Yang, P.; Zhang, Z.; Sun, M.; Lin, F.; Cheng, T.; Shi, J.; Xie, C.; Shi, Y.; Jiang, S.; Huan, Y.; Liu, P.; Ding, F.; Xiong, C.; Xie, D.; Zhang, Y. Thickness Tunable Wedding-Cake-like MoS₂ Flakes for High-Performance Optoelectronics. *ACS Nano* **2019**, *13*, 3649–3658.
- (3) Shin, D.; Hübener, H.; De Giovannini, U.; Jin, H.; Rubio, A.; Park, N. Phonon-Driven Spin-Floquet Magneto-Valleytronics in MoS₂. *Nat. Commun.* **2018**, *9*, No. 638.
- (4) Schaibley, J. R.; Yu, H.; Clark, G.; Rivera, P.; Ross, J. S.; Seyler, K. L.; Yao, W.; Xu, X. Valleytronics in 2D Materials. *Nat. Rev. Mater.* **2016**, *1*, No. 16055.
- (5) Han, S. S.; Kim, J. H.; Noh, C.; Kim, J. H.; Ji, E.; Kwon, J.; Yu, S. M.; Ko, T. J.; Okogbue, E.; Oh, K. H.; Chung, H.-S.; Jung, Y.; Lee, G.-H.; Jung, Y. Horizontal-to-Vertical Transition of 2D Layer Orientation in Low-Temperature Chemical Vapor Deposition-Grown PtSe₂ and Its Influences on Electrical Properties and Device Applications. ACS Appl. Mater. Interfaces 2019, 11, 13598–13607.

- (6) Zhao, Y.; Qiao, J.; Yu, Z.; Yu, P.; Xu, K.; Lau, S. P.; Zhou, W.; Liu, Z.; Wang, X.; Ji, W.; Chai, Y. High-Electron-Mobility and Air-Stable 2D Layered PtSe, FETs. Adv. Mater. 2017, 29, No. 1604230.
- (7) Okogbue, E.; Han, S. S.; Ko, T. J.; Chung, H. S.; Ma, J.; Shawkat, M. S.; Kim, J. H.; Kim, J. H.; Ji, E.; Oh, K. H.; Zhai, L.; Lee, G.-H.; Jung, Y. Multifunctional Two-Dimensional PtSe₂-Layer Kirigami Conductors with 2000% Stretchability and Metallic-to-Semiconducting Tunability. *Nano Lett.* **2019**, *19*, 7598–7607.
- (8) Wang, Y.; Li, L.; Yao, W.; Song, S.; Sun, J. T.; Pan, J.; Ren, X.; Li, C.; Okunishi, E.; Wang, Y. Q.; Wang, E.; Shao, Y.; Zhang, Y. Y.; Yang, H.-T.; Schwier, E. F.; Iwasawa, H.; Shimada, K.; Taniguchi, M.; Cheng, Z.; Zhou, S.; Du, S.; Pennycook, S. J.; Pantelides, S. T.; Gao, H.-J. Monolayer PtSe₂, a New Semiconducting Transition-Metal-Dichalcogenide, Epitaxially Grown by Direct Selenization of Pt. *Nano Lett.* 2015, 15, 4013–4018.
- (9) Yao, W.; Wang, E.; Huang, H.; Deng, K.; Yan, M.; Zhang, K.; Miyamoto, K.; Okuda, T.; Li, L.; Wang, Y.; Gao, H.; Liu, C.; Duan, W.; Zhou, S. Direct Observation of Spin-Layer Locking by Local Rashba Effect in Monolayer Semiconducting PtSe₂ Film. *Nat. Commun.* **2017**, *8*, No. 14216.
- (10) Shawkat, M. S.; Chung, H.-S.; Dev, D.; Das, S.; Roy, T.; Jung, Y. Two-Dimensional/Three-Dimensional Schottky Junction Photovoltaic Devices Realized by the Direct CVD Growth of VdW 2D PtSe₂ Layers on Silicon. ACS Appl. Mater. Interfaces **2019**, 11, 27251–27258.
- (11) Yu, X.; Yu, P.; Wu, D.; Singh, B.; Zeng, Q.; Lin, H.; Zhou, W.; Lin, J.; Suenaga, K.; Liu, Z.; Wang, Q. J. Atomically Thin Noble Metal Dichalcogenide: A Broadband Mid-Infrared Semiconductor. *Nat. Commun.* **2018**, *9*, No. 1545.
- (12) Su, T. Y.; Medina, H.; Chen, Y. Z.; Wang, S. W.; Lee, S. S.; Shih, Y. C.; Chen, C. W.; Kuo, H. C.; Chuang, F. C.; Chueh, Y. L. Phase-Engineered PtSe₂-Layered Films by a Plasma-Assisted Selenization Process toward All PtSe₂-Based Field Effect Transistor to Highly Sensitive, Flexible, and Wide-Spectrum Photoresponse Photodetectors. *Small* **2018**, *14*, No. 1800032.
- (13) Politano, A.; Chiarello, G.; Ghosh, B.; Sadhukhan, K.; Kuo, C. N.; Lue, C. S.; Pellegrini, V.; Agarwal, A. 3D Dirac Plasmons in the Type-II Dirac Semimetal PtTe₂. *Phys. Rev. Lett.* **2018**, *121*, No. 086804.
- (14) Deng, K.; Yan, M.; Yu, Z.; Li, J.; Zhou, X.; Zhang, K.; Zhao, Y.; Miyamoto, K.; Okuda, T.; Duan, W.; Wu, Y.; Zhong, X.; Zhou, S. Crossover from 2D Metal to 3D Dirac Semimetal in Metallic PtTe₂ Films with Local Rashba Effect. Sci. Bull. **2019**, 64, 1044–1048.
- (15) Fu, D.; Bo, X.; Fei, F.; Wu, B.; Gao, M.; Wang, X.; Naveed, M.; Shah, S. A.; Bu, H.; Wang, B.; Cao, L.; Zou, W.; Wan, X.; Song, F. Quantum Oscillations in Type-II Dirac Semimetal PtTe₂. *Phys. Rev. B* **2018**, 97, No. 245109.
- (16) Zhang, K.; Yan, M.; Zhang, H.; Huang, H.; Arita, M.; Sun, Z.; Duan, W.; Wu, Y.; Zhou, S. Experimental Evidence for Type-II Dirac Semimetal in PtSe₂. *Phys. Rev. B* **2017**, *96*, No. 125102.
- (17) Huang, H.; Zhou, S.; Duan, W. Type-II Dirac Fermions in the PtSe₂ Class of Transition Metal Dichalcogenides. *Phys. Rev. B* **2016**, 94, No. 121117(R).
- (18) Bahramy, M. S.; Clark, O. J.; Yang, B. J.; Feng, J.; Bawden, L.; Riley, J. M.; Markovic, I.; Mazzola, F.; Sunko, V.; Biswas, D.; Cooil, S. P.; Jorge, M.; Wells, J. W.; Leandersson, M.; Balasubramanian, T.; Fujii, J.; Vobornik, I.; Rault, J. E.; Kim, T. K.; Hoesch, M.; Okawa, K.; Asakawa, M.; Sasagawa, T.; Eknapakul, T.; Meevasana, W.; King, P. D. C. Ubiquitous Formation of Bulk Dirac Cones and Topological Surface States from a Single Orbital Manifold in Transition-Metal Dichalcogenides. *Nat. Mater.* 2018, 17, 21–27.
- (19) Yan, M.; Huang, H.; Zhang, K.; Wang, E.; Yao, W.; Deng, K.; Wan, G.; Zhang, H.; Arita, M.; Yang, H.; Sun, Z.; Yao, H.; Wu, Y.; Fan, S.; Duan, W.; Zhou, S. Lorentz-Violating Type-II Dirac Fermions in Transition Metal Dichalcogenide PtTe₂. Nat. Commun. 2017, 8, No. 257.
- (20) Villaos, R. A. B.; Crisostomo, C. P.; Huang, Z.-Q.; Huang, S.-M.; Padama, A. A. B.; Albao, M. A.; Lin, H.; Chuang, F.-C. Thickness

- Dependent Electronic Properties of Pt Dichalcogenides. *npj 2D Mater. Appl.* **2019**, *3*, No. 2.
- (21) Fu, L.; Hu, D.; Mendes, R. G.; Rümmeli, M. H.; Dai, Q.; Wu, B.; Fu, L.; Liu, Y. Highly Organized Epitaxy of Dirac Semimetallic PtTe₂ Crystals with Extrahigh Conductivity and Visible Surface Plasmons at Edges. *ACS Nano* **2018**, *12*, 9405–9411.
- (22) Ma, H.; Chen, P.; Li, B.; Li, J.; Ai, R.; Zhang, Z.; Sun, G.; Yao, K.; Lin, Z.; Zhao, B.; Wu, R.; Tang, X.; Duan, X.; Duan, X. Thickness-Tunable Synthesis of Ultrathin Type-II Dirac Semimetal PtTe₂ Single Crystals and Their Thickness-Dependent Electronic Properties. *Nano Lett.* **2018**, *18*, 3523–3529.
- (23) Hao, S.; Zeng, J.; Xu, T.; Cong, X.; Wang, C.; Wu, C.; Wang, Y.; Liu, X.; Cao, T.; Su, G.; Jia, L.; Wu, Z.; Lin, Q.; Zhang, L.; Yan, S.; Guo, M.; Wang, Z.; Tan, P.; Sun, L.; Ni, Z.; Liang, S.-J.; Cui, X.; Miao, F. Low-Temperature Eutectic Synthesis of PtTe₂ with Weak Antilocalization and Controlled Layer Thinning. *Adv. Funct. Mater.* **2018**, 28, No. 1803746.
- (24) Chia, X.; Sofer, Z.; Luxa, J.; Pumera, M. Layered Noble Metal Dichalcogenides: Tailoring Electrochemical and Catalytic Properties. *ACS Appl. Mater. Interfaces* **2017**, *9*, 25587–25599.
- (25) Chia, X.; Adriano, A.; Lazar, P.; Sofer, Z.; Luxa, J.; Pumera, M. Layered Platinum Dichalcogenides (PtS₂, PtSe₂, and PtTe₂) Electrocatalysis: Monotonic Dependence on the Chalcogen Size. *Adv. Funct. Mater.* **2016**, *26*, 4306–4318.
- (26) Jung, Y.; Shen, J.; Liu, Y.; Woods, J. M.; Sun, Y.; Cha, J. J. Metal Seed Layer Thickness-Induced Transition from Vertical to Horizontal Growth of MoS₂ and WS₂. *Nano Lett.* **2014**, *14*, 6842–6849.
- (27) Ji, Q.; Li, C.; Wang, J.; Niu, J.; Gong, Y.; Zhang, Z.; Fang, Q.; Zhang, Y.; Shi, J.; Liao, L.; Wu, X.; Gu, L.; Liu, Z.; Zhang, Y. Metallic Vanadium Disulfide Nanosheets as a Platform Material for Multifunctional Electrode Applications. *Nano Lett.* **2017**, *17*, 4908–4916.
- (28) Acerce, M.; Voiry, D.; Chhowalla, M. Metallic 1T Phase MoS₂ Nanosheets as Supercapacitor Electrode Materials. *Nat. Nanotechnol.* **2015**, *10*, 313–318.
- (29) Park, S.; Ruoff, R. S. Chemical Methods for the Production of Graphenes. *Nat. Nanotechnol.* **2009**, *4*, 217–224.
- (30) Gaur, A. P. S.; Sahoo, S.; Ahmadi, M.; Dash, S. P.; Guinel, M. J. F.; Katiyar, R. S. Surface Energy Engineering for Tunable Wettability through Controlled Synthesis of MoS₂. *Nano Lett.* **2014**, *14*, 4314–4321
- (31) Chow, P. K.; Singh, E.; Viana, B. C.; Gao, J.; Luo, J.; Li, J.; Lin, Z.; Elías, A. L.; Shi, Y.; Wang, Z.; Terrones, M.; Koratkar, N. Wetting of Mono and Few-Layered WS₂ and MoS₂ Films Supported on Si/SiO₂ Substrates. *ACS Nano* **2015**, *9*, 3023–3031.
- (32) Son, S. B.; Kim, Y.; Kim, A.; Cho, B.; Hong, W.-K. Ultraviolet Wavelength-Dependent Optoelectronic Properties in Two-Dimensional NbSe₂–WSe₂ Van Der Waals Heterojunction-Based Field-Effect Transistors. ACS Appl. Mater. Interfaces 2017, 9, 41537–41545.
- (33) Choudhary, N.; Chung, H. S.; Kim, J. H.; Noh, C.; Islam, M. A.; Oh, K. H.; Coffey, K.; Jung, Y. J. Y.; Jung, Y. J. Y. Strain-Driven and Layer-Number-Dependent Crossover of Growth Mode in van Der Waals Heterostructures: 2D/2D Layer-By-Layer Horizontal Epitaxy to 2D/3D Vertical Reorientation. *Adv. Mater. Interfaces* 2018, 5, No. 1800382.
- (34) Wang, L.; Zihlmann, S.; Liu, M. H.; Makk, P.; Watanabe, K.; Taniguchi, T.; Baumgartner, A.; Schönenberger, C. New Generation of Moiré Superlattices in Doubly Aligned HBN/Graphene/HBN Heterostructures. *Nano Lett.* **2019**, *19*, 2371–2376.
- (35) Deokar, G.; Rajput, N. S.; Vancsó, P.; Ravaux, F.; Jouiad, M.; Vignaud, D.; Cecchet, F.; Colomer, J. F. Large Area Growth of Vertically Aligned Luminescent MoS₂ Nanosheets. *Nanoscale* **2017**, *9*, 277–287.
- (36) Stern, C.; Grinvald, S.; Kirshner, M.; Sinai, O.; Oksman, M.; Alon, H.; Meiron, O. E.; Bar-Sadan, M.; Houben, L.; Naveh, D. Growth Mechanisms and Electronic Properties of Vertically Aligned MoS₂. Sci. Rep. **2018**, 8, No. 16480.
- (37) Bauer, E.; Poppa, H. Recent Advances in Epitaxy. *Thin Solid Films* **1972**, *12*, 167–185.

- (38) Grabow, M. H.; Gilmer, G. H. Thin Film Growth Modes, Wetting and Cluster Nucleation. Surf. Sci. 1988, 194, 333-346.
- (39) Lang, O.; Schlaf, R.; Tomm, Y.; Pettenkofer, C.; Jaegermann, W. Single Crystalline GaSe/WSe₂ heterointerfaces Grown by van Der Waals Epitaxy. I. Growth Conditions. *J. Appl. Phys.* **1994**, *75*, 7805–7813.
- (40) Schell-Sorokin, A. J.; Tromp, R. M. Mechanical Stresses in (Sub)Monolayer Epitaxial Films. *Phys. Rev. Lett.* **1990**, *64*, 1039–1042.
- (41) Thompson, C. V.; Floro, J.; Smith, H. I. Epitaxial Grain Growth in Thin Metal Films. *J. Appl. Phys.* **1990**, *67*, 4099–4104.
- (42) Kim, K.-H. Digital Micrograph Script Source Listing for a Geometric Phase Analysis. *Appl. Microsc.* **2015**, *45*, 101–105.
- (43) Hÿtch, M. J.; Snoeck, E.; Kilaas, R. Quantitative Measurement of Displacement and Strain Fields from HREM Micrographs. *Ultramicroscopy* **1998**, *74*, 131–146.
- (44) Elibol, K.; Susi, T.; O'Brien, M.; Bayer, B. C.; Pennycook, T. J.; McEvoy, N.; Duesberg, G. S.; Meyer, J. C.; Kotakoski, J. Grain Boundary-Mediated Nanopores in Molybdenum Disulfide Grown by Chemical Vapor Deposition. *Nanoscale* **2017**, *9*, 1591–1598.
- (45) Sun, C.; Paulauskas, T.; Sen, F. G.; Lian, G.; Wang, J.; Buurma, C.; Chan, M. K. Y.; Klie, R. F.; Kim, M. J. Atomic and Electronic Structure of Lomer Dislocations at CdTe Bicrystal Interface. *Sci. Rep.* **2016**, *6*, No. 27009.
- (46) Kresse, G.; Joubert, D. From Ultrasoft Pseudopotentials to the Projector Augmented-Wave Method. *Phys. Rev. B: Condens. Matter Mater. Phys.* **1999**, *59*, 1758–1775.
- (47) Ciarrocchi, A.; Avsar, A.; Ovchinnikov, D.; Kis, A. Thickness-Modulated Metal-to-Semiconductor Transformation in a Transition Metal Dichalcogenide. *Nat. Commun.* **2018**, *9*, No. 919.
- (48) Yu, Y.; Huang, S. Y.; Li, Y.; Steinmann, S. N.; Yang, W.; Cao, L. Layer-Dependent Electrocatalysis of MoS₂ for Hydrogen Evolution. *Nano Lett.* **2014**, *14*, 553–558.
- (49) Cappelluti, E.; Roldán, R.; Silva-Guillén, J. A.; Ordejón, P.; Guinea, F. Tight-Binding Model and Direct-Gap/Indirect-Gap Transition in Single-Layer and Multilayer MoS₂. *Phys. Rev. B: Condens. Matter Mater. Phys.* **2013**, 88, No. 075409.
- (50) Zhang, Z.; Niu, J.; Yang, P.; Gong, Y.; Ji, Q.; Shi, J.; Fang, Q.; Jiang, S.; Li, H.; Zhou, X.; Gu, L.; Wu, X.; Zhang, Y. Van Der Waals Epitaxial Growth of 2D Metallic Vanadium Diselenide Single Crystals and Their Extra-High Electrical Conductivity. *Adv. Mater.* **2017**, 29, No. 1702359.
- (51) Choi, B. K.; Lee, I. H.; Kim, J.; Chang, Y. J. Tunable Wetting Property in Growth Mode-Controlled WS₂ Thin Films. *Nanoscale Res. Lett.* **2017**, *12*, No. 262.
- (52) Kozbial, A.; Li, Z.; Conaway, C.; McGinley, R.; Dhingra, S.; Vahdat, V.; Zhou, F.; D'Urso, B.; Liu, H.; Li, L. Study on the Surface Energy of Graphene by Contact Angle Measurements. *Langmuir* **2014**, *30*, 8598–8606.
- (53) Kumar, P.; Viswanath, B. Horizontally and Vertically Aligned Growth of Strained MoS₂ Layers with Dissimilar Wetting and Catalytic Behaviors. *CrystEngComm* **2017**, *19*, 5068–5078.
- (54) Agrawal, A. V.; Kumar, N.; Venkatesan, S.; Zakhidov, A.; Manspeaker, C.; Zhu, Z.; Hernandez, F. R.; Bao, J.; Kumar, M. Controlled Growth of MoS₂ Flakes from In-Plane to Edge-Enriched 3D Network and Their Surface-Energy Studies. *ACS Appl. Nano Mater.* **2018**, *1*, 2356–2367.
- (55) Quéré, D. Wetting and Roughness. *Annu. Rev. Mater. Res.* **2008**, 38, 71–99.
- (56) Owens, D. K.; Wendt, R. C. Estimation of the Surface Free Energy of Polymers. *J. Appl. Polym. Sci.* **1969**, *13*, 1741–1747.
- (57) Guo, G. Y.; Liang, W. Y. The Electronic Structures of Platinum Dichalcogenides: PtS₂, PtSe₂ and PtTe₂. *J. Phys. C: Solid State Phys.* **1986**, *19*, 995–1008.
- (58) Li, Y. X.; Putungan, D. B.; Lin, S. H. Two-Dimensional MTe2 (M = Co, Fe, Mn, Sc, Ti) Transition Metal Tellurides as Sodium Ion Battery Anode Materials: Density Functional Theory Calculations. *Phys. Lett. A* **2018**, 382, 2781–2786.

- (59) Blöchl, P. E. Projector Augmented-Wave Method. *Phys. Rev. B* **1994**, *50*, 17953–17979.
- (60) Kresse, G.; Furthmüller, J. Efficient Iterative Schemes for Ab Initio Total-Energy Calculations Using a Plane-Wave Basis Set. *Phys. Rev. B: Condens. Matter Mater. Phys.* **1996**, *54*, 11169–11186.
- (61) Klimeš, J.; Bowler, D. R.; Michaelides, A. Chemical Accuracy for the van Der Waals Density Functional. *J. Phys.: Condens. Matter* **2010**, 22, No. 022201.
- (62) Klime, J.; Bowler, D. R.; Michaelides, A. Van Der Waals Density Functionals Applied to Solids. *Phys. Rev. B: Condens. Matter Mater. Phys.* **2011**, 83, No. 195131.
- (63) Hunter, J. D. Matplotlib: A 2D Graphics Environment. *Comput. Sci. Eng.* **2007**, *9*, 90–95.